








Article

Numerical and Experimental Investigation of Different Oil Levels and Operation Conditions on the Individual Hydraulic Losses of Spherical Rolling Bearings

Thomas Christoph Petrzik ^{1,*}, Kim Marius Brill ², Georg Jacobs ¹, Oliver Koch ², Benjamin Lehmann ¹, Peter Rößler ¹ and Amirreza Niazmehr ¹

¹ Institute for Machine Elements and Systems Engineering, RWTH Aachen University, 52062 Aachen, Germany

² Institute MEGT, RPTU University of Kaiserslautern-Landau, 67663 Kaiserslautern, Germany

* Correspondence: thomas.petrzik@imse.rwth-aachen.de

Abstract

Improving the energy efficiency of rolling bearings requires a component-resolved understanding of loss mechanisms. While analytical models capture load-dependent losses, load-independent hydraulic losses demand a physics-based approach. This paper presents a computational fluid dynamics (CFD) methodology for the qualification of individual hydraulic loss contributions and to assess their sensitivity to operating conditions. The approach decomposes the total hydraulic loss of the spherical roller bearing 22320 into component-level shares and is benchmarked against dedicated experiments. The simulated results show good agreement with experimental measurements, supporting the validity of the methodology. The discrepancy between the measured and simulated friction torque values averaged at 2–7%, with a single outlier. Furthermore, CFD methods have been demonstrated to be capable of predicting trends in hydraulic losses resulting from variations in speed and temperature. A consistent finding across all investigated conditions is that the rolling elements dominate the hydraulic losses. Churning-induced losses of the rolling elements contribute for more than 50% of the hydraulic losses of the hole bearing in every test. The proposed methodology offers a reproducible way to assign losses individually, compare operating scenarios and guide targeted design measures for loss reduction in rolling bearings. Furthermore, dynamic kinematic simulations of rolling bearings can be equipped with component-resolved hydraulic losses. This is enabling more accurate predictive modelling of the bearing kinematics and detecting effects such as slippage.

Keywords: hydraulic losses; spherical roller bearings; computational fluid dynamics; two-phase simulation; friction measurement; OpenFOAM



Received: 28 November 2025

Revised: 23 December 2025

Accepted: 25 December 2025

Published: 30 December 2025

Copyright: © 2025 by the authors.

Licensee MDPI, Basel, Switzerland.

This article is an open access article

distributed under the terms and

conditions of the [Creative Commons](https://creativecommons.org/licenses/by/4.0/)

[Attribution \(CC BY\)](https://creativecommons.org/licenses/by/4.0/) license.

1. Introduction

The total power loss of a rolling bearing can be decomposed into two parts [1,2]. The first part is the load-dependent losses, which arise from contact mechanics and material hysteresis, primarily rolling, sliding, and spin friction (F_{μ}) of the interacting components (see Figure 1). Load-independent losses (hereinafter: hydraulic losses) result from the fluid–structure interaction between lubricant and moving parts and can be further separated into drag and churning losses. Drag losses are associated with the displacement of the lubricant by the translating rolling elements [1–4]. Drag losses result in a force that slows down the rolling element in its translational movement through the bearing,

whereas churning losses result from viscous shear within the lubricant driven by rotating components [1–4]. Churning losses result in a torque that slows down the components rotational speed around its own axis.

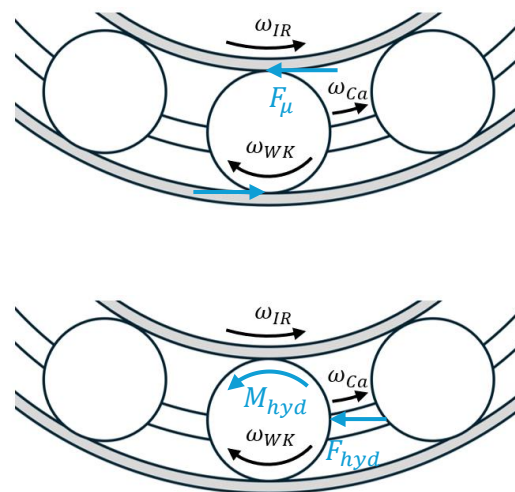


Figure 1. Power loss inducing forces and torques inside a bearing with 1: load-dependent force (F_μ) as a result of friction and hysteresis effects; 2: hydraulic forces, drag (F_{hyd}) as a result of the displacement of the lubricant and churning (M_{hyd}) as a result of shearing of the lubricant.

A broad spectrum of methods exists to predict load-dependent and hydraulic losses. For the load-dependent losses, analytical models on contact level typically provide sufficient accuracy [5–7]. In contrast, hydraulic losses are often estimated using manufacturer correlations (e.g., the widely used SKF formulation [8]), empirical fits, or numerical approaches such as computational fluid dynamics (CFD). While convenient, the SKF equation, which is derived from aggregated experiments, tends to lose accuracy at higher speeds and does not resolve the individual drag and churning contributions [9,10]. A component-wise perspective is therefore desirable. It provides mechanistic insight and enables targeted design measures to improve bearing efficiency by quantifying how component-specific modifications affect both component- and system-level losses. Moreover, the component-resolved hydraulic analysis can be integrated into multibody kinematic simulations, which typically neglect hydraulic losses, thereby increasing their fidelity. Consequently, contemporary CFD studies increasingly report component-resolved hydraulic losses rather than a single aggregated quantity [11].

The CFD literature on hydraulic losses has expanded steadily in recent years [12]. Two main strategies can be distinguished. First, “reduced” models determine drag coefficients as a function of the Reynolds number for simplified geometries (e.g., one to three cylinders in a box) and map them back to bearings [13,14]. Second, “single-chamber” models simulate a representative bearing sector (often exploiting geometric periodicity) to compute P_{hydr} for flooded conditions [1,15,16]. However, most of these studies assume a fully flooded bearing; therefore, most of these studies conduct a single-phase (oil) flow simulation. When the fill level varies, a two-phase treatment (oil–air) with free-surface dynamics becomes necessary to capture drag/churning partitioning and level-dependent effects.

The simplifications mentioned above are particularly restrictive for spherical roller bearings (SRBs) that are not fully flooded. Radial symmetry cannot represent different oil levels around the circumference, and axial symmetry is compromised by the barrel geometry, the inherent ring angle, and the staggered arrangement of the two roller rows. As a result, methods relying on periodic sectors are of limited applicability to partially filled SRBs and full-bearing models are warranted. Despite extensive CFD work on tapered

roller bearings, ball bearings, and cylindrical roller bearings, SRBs remain comparatively underexplored in this regard.

Motivated by this gap, the present study develops a two-phase CFD model of a complete, oil-bath-lubricated, two-row spherical roller bearing (type 22320). The objectives are as follows: 1. Resolve hydraulic losses at the component level (rolling elements, inner ring, cage) by separately quantifying drag and churning 2. Validate total hydraulic losses against experiments 3. Assess the influence of operating parameters—inner-ring speed, lubricant temperature, and fill level—on the distribution and magnitude of hydraulic losses.

2. Materials and Methods

2.1. Experimental Approach

2.1.1. Test Rig

The friction torque measurements were conducted using the MEGT friction torque test rig. Originally developed within the scope of AUL'S work [17], the rig has been employed in numerous research projects over the years and has consistently demonstrated its reliability [17–22]. The friction torque test bench has a modular design for investigating bearings with bore diameters from 40 mm to outer diameters up to 215 mm. Adjustable parameters include speed, radial and axial force, inclination, and angular deviation. A sealed oil chamber allows oil level control up to a fully flooded bearing. You can see the test bench setup in Figure 2.

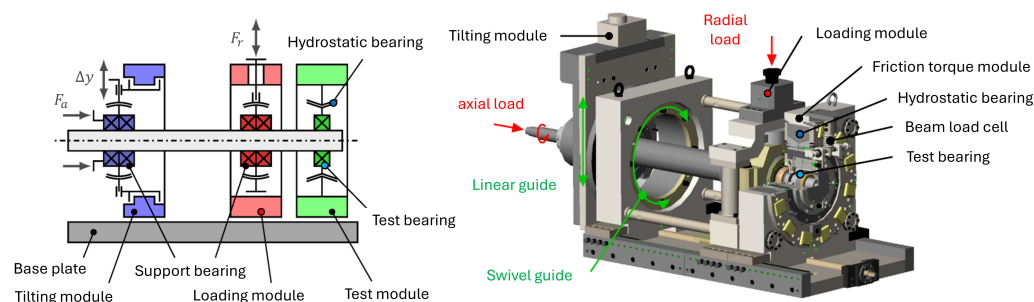


Figure 2. Design of the friction torque test bench.

The horizontal drive shaft passes through three modules: tilting, loading, and test module. Radial force is applied by four spindle bearings in O-arrangement via a screw and disc spring mechanism, measured by a force sensor. Axial force is introduced hydraulically in the tilting module and transmitted through the shaft to the test bearing. All modules are mounted on a base plate, with the load module position adjustable via spindle drive. Shaft inclination is achieved through a dovetail linear guide and lead screw.

Friction torque is measured with a hydrostatically mounted sleeve connected to a lever arm and force sensor, which together enable precise torque determination.

2.1.2. Test Procedure

A spherical roller bearing of size 22320 was selected for experimental investigation. The aim of the test series was to analyse the influence of fill level, oil temperature, and inner-ring speed on the total friction torque of the bearing. The results were then compared with those of existing calculation methods, such as the quasi-static bearing tool Bearinx Online, as well as the catalogue methods of SKF and Schaeffler.

The investigations followed a full factorial test plan, systematically varying the influencing variables of speed, oil level, and temperature. The exact operating parameters for the bearing can be viewed in Table 1. The radial load was limited to the respective minimum load of the test bearing to specifically map the critical operating range. The shaft

speed was selected in three stages depending on the thermal reference speed n_{θ} ($0.4 \cdot n_{\theta}$, $0.8 \cdot n_{\theta}$, $1.0 \cdot n_{\theta}$).

Table 1. Operating parameter space for experiments and simulations of the SRB.

Radial Force [kN]	Shaft Speed [rpm]	Oil Temperature [°C]	Oil Hight [mm]	CFD Operation Point
8.4	960 rpm	50 °C	2 mm	-
8.4	960 rpm	50 °C	13.5 mm	1
8.4	960 rpm	50 °C	46 mm	2
8.4	960 rpm	50 °C	92 mm	3
8.4	960 rpm	70 °C	2 mm	-
8.4	960 rpm	70 °C	13.5 mm	4
8.4	960 rpm	70 °C	46 mm	5
8.4	960 rpm	70 °C	92 mm	6
8.4	1920 rpm	50 °C	2 mm	-
8.4	1920 rpm	50 °C	13.5 mm	7
8.4	1920 rpm	50 °C	46 mm	8
8.4	1920 rpm	50 °C	92 mm	9

The lubricant level was set in four stages:

- Minimum quantity (MIN): 2 mm;
- Oil level up to the middle of the lowest rolling element (MWK): 13.5 mm;
- Bearing quartered in oil (QB): 46 mm;
- Bearing half in oil (HB): 92 mm.

The reference point for the oil level was defined at the lowest point of the outer-ring raceway.

An unadditivated mineral oil of ISO VG 100, with kinematic viscosities of $\nu_{40^{\circ}\text{C}} = 94.02 \text{ mm}^2 \text{ s}^{-1}$ and $\nu_{100^{\circ}\text{C}} = 10.09 \text{ mm}^2 \text{ s}^{-1}$, was used. Additional lubricant properties are provided in Table 2.

Table 2. Parameters for viscosity according to DICKE and VOGEL for reference oil FVA No. 3 (measured in [23]).

Parameter	Variable	Value	Unit
Temperature parameter	K	0.062	mPa s
Temperature parameter	B	1021.7	°C
Temperature parameter	C	101.5517	°C
Pressure parameter	a_1	327.7918	bar
Pressure parameter	a_2	2.9862	bar °C ⁻¹
Pressure parameter	b_1	4.419×10^{-3}	-
Pressure parameter	b_2	3.0115×10^{-4}	°C ⁻¹
Density at 15 °C	ρ	887.6	kg m ⁻³
Thermal conductivity	λ	0.134	W m ⁻¹ K ⁻¹
Temperature density coefficient	α	-6×10^{-4}	g mL ⁻¹ K ⁻¹

The oil temperatures were set by speeding up the bearing to reach the target temperature. The shaft speed was then adjusted to the respective test parameter. The oil temperature was measured in the oil bath and at the outer ring, next to the location with the highest contact pressure. For minimum quantity lubrication, only the temperature of the outer ring was used, as there was no oil bath here.

The following variables were recorded during the tests:

- Shaft speed;
- Cage speed of the front cage;

- Radial force;
- Bearing friction torque on the outer ring;
- Temperature of the oil bath;
- Outer-ring temperature at the lowest point.

The combination of parameter levels resulted in 12 different operating points. This provided a comprehensive database for analysis and comparison with the simulation and catalog methods.

2.2. Numerical Approach

2.2.1. Simulation Setup

OpenFOAM v11, a free and open-source software, is employed to perform numerical simulations. Before simulation, a computational mesh of the bearing was generated. Initially, the CAD geometry of the bearing was reconstructed based on measurement data obtained at the Chair of Machine Elements and Gear Technology (MEGT). A sketch of the outer-ring-guided cage spherical roller bearing is shown in Figure 3, with the transmitted geometric dimensions in Table 3.

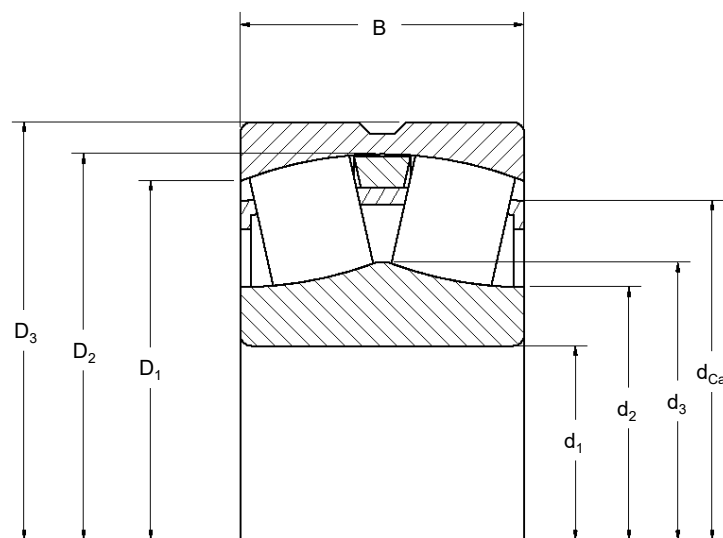


Figure 3. Sketch of the spherical roller bearing 22320.

Table 3. Geometric dimensions of the spherical roller bearing 22320.

Denotation	Symbol	Value [mm]
Bearing outer diameter	D_3	215.0
Outer-ring raceway diameter	D_2	197.9
Outer-ring raceway diameter	D_1	184.7
Inner-ring raceway diameter	d_3	130.0
Inner-ring raceway diameter	d_2	143.6
Inner-ring bore diameter	d_1	100.0
Cage outer diameter	d_{Ca}	148.6
Bearing width	B	73.0
Rolling-element diameter	d_{WK}	26.3
Rolling-element length	l_{WK}	30.6

In the process, geometric simplifications were applied, including the removal of roundings and chambers. This simplification assumes that these geometries hardly affect the global flow of the lubricant. While the literature shows that geometric simplifications like neglecting rounding radii do not significantly affect the result of hydraulic losses, they do

lead to a reduction in calculation time and mesh generation [16]. Furthermore, FELDERMANN'S [1] approach for the hole bearing model was adopted and expanded to enable two-phase simulations. In his approach, the lubrication gap between the rolling elements and the inner or outer ring are neglected. This assumption is based on two theoretical considerations. First, the volumetric flow through the lubrication gap is small compared with the surrounding flow, so its influence on the global flow field and thus on the formation of hydraulic losses, is negligible. Second, in the lubrication gap, there is no displacement of the lubricant; therefore, drag losses can be neglected. As the lubricant is accelerated within the lubrication gap, the relative velocity between the fluid and the component surface decreases, which reduces the effective shear and, consequently, the associated churning losses. Since the cells that would otherwise be generated in the lubrication gap are small compared to the rest of the mesh, their inclusion would significantly increase the simulation time without providing substantial additional value; therefore, they are omitted [1]. The width of the gap is not a fixed value, but is determined by the minimum cell size and the requirement that there are five cells between the inner/outer ring and the rolling element. This allows for stable numerical calculations. A study to investigate the influence of gap width on the result was not conducted, as it can be assumed from the extant literature that the influence of the gap on the hydraulic losses of the overall system is negligible. The resulting CAD file can be seen in Figure 4.

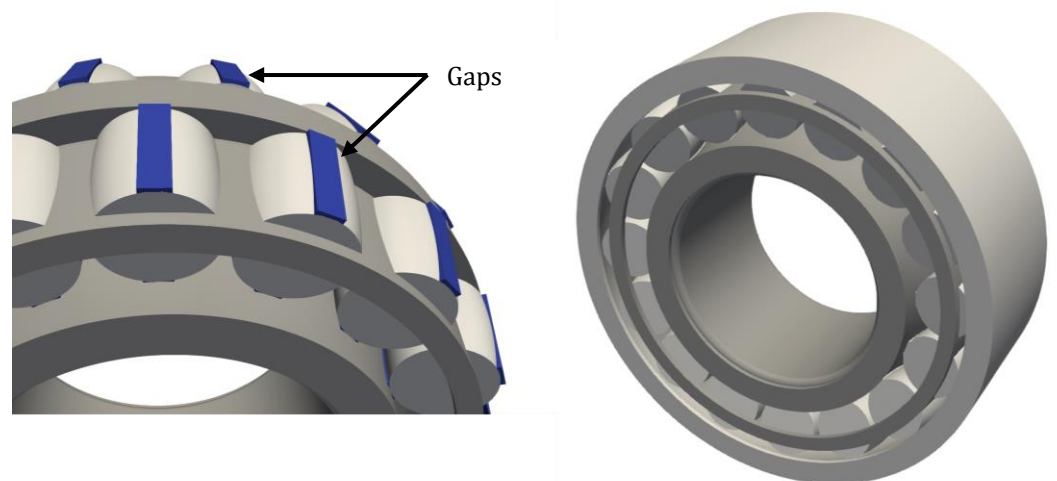


Figure 4. CAD file used to generate the fluid space. **Left:** generated CAD geometry of the spherical roller bearing 22320 with invisible outer ring; highlighted are the areas where the lubrication gaps are neglected. **Right:** hole CAD file with the implemented simplifications.

Subsequently, the blockMesh utility was employed to create a structured background mesh, which served as the base for further refinement. Using snappyHexMesh, a negative imprint of the CAD file was generated, enabling the extraction of the fluid domain. During this process, inflation layers (also referred to as boundary layers) were added to the surfaces of the bearing components to accurately capture near-wall flow behaviour and shear effects. Finally, the mesh was refined to resolve the flow-relevant regions within the fluid space with high accuracy. The surface mesh is visible on the left of Figure 5. On the right is a cross-section of the model showing the interior of the model. The cut-out rolling elements and the cage surrounded by the mesh are visible. The inserted inflation layers are also visible around the rolling elements and the inner and outer ring. The mesh becomes coarser as the distance to moving surfaces increases. This cell growth was adjusted because the velocity gradients decrease with increasing distance and a coarser mesh is sufficient for consistent accuracy. The coarser mesh reduces the required computing time.

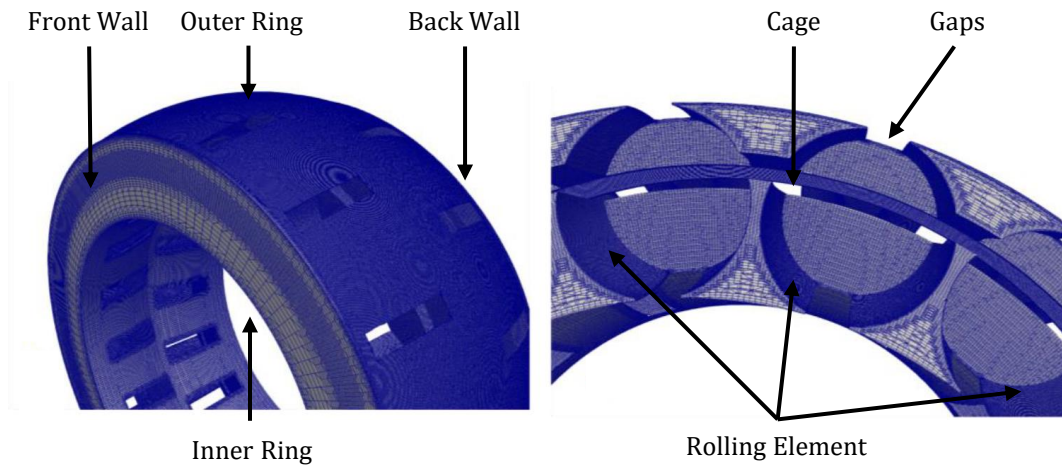


Figure 5. Left: Resulting mesh of the bearing 22320. Right: Cut to show inside of the mesh.

As mentioned, the static mesh approach is utilized to reduce the time taken for calculations (compared to a dynamic mesh approach, where parts of the mesh are moving during the simulation). In order to map the movements of the rolling bearing realistically, the following view is applied: The observer moves with the rotational speed of the cage of the rolling bearing. Consequently, the rolling elements and the cage no longer move translatorily around the shaft axis (orbit rotation). The rolling elements rotate exclusively around their own axis. The velocity of the oil bath and the inner and outer ring are modified to the relative speed. An overview of the kinematics used in the simulations is provided in Figure 6. The absolute angular speed of the inner ring, ω_{IR} , is reduced by the cage speed ω_{Ca} to yield the relative speed $\omega_{IR,rel}$. The fluid in the oil bath and the inner and outer ring are stationary in the absolute view. Therefore, in the relative view, they appear to rotate with the speeds ω_{Fl} and $\omega_{AR,rel}$, respectively.

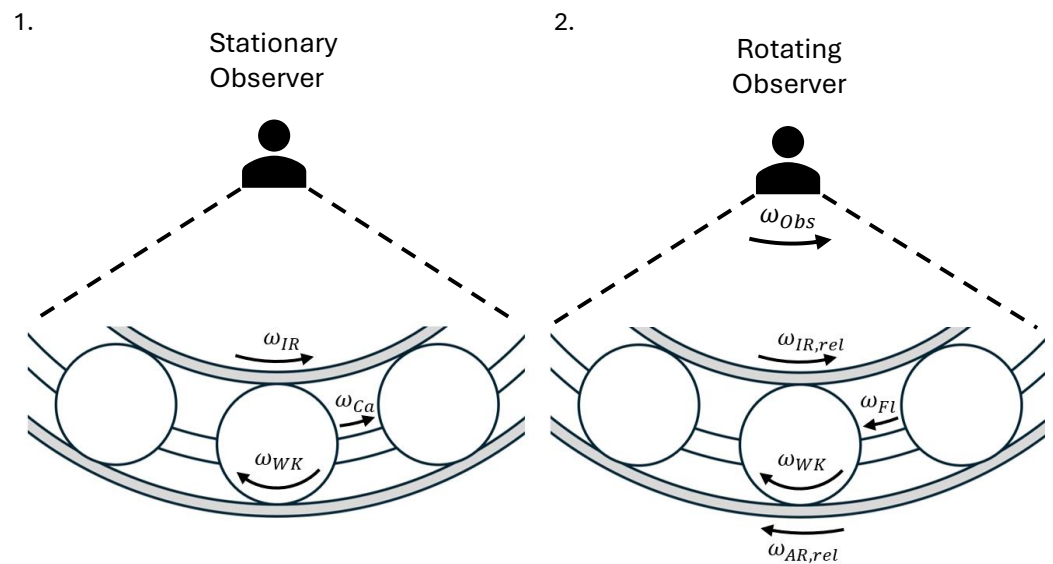


Figure 6. (1): Absolute consideration of speeds in the rolling bearing. (2): Relative consideration of speeds with rotating observer used for simulation.

The boundary conditions resulting from the relative consideration are shown in Table 4. Under U are the boundary conditions representing the velocity. p_{rgh} denotes the modified pressure field in which the hydrostatic contribution of gravity is subtracted from the absolute pressure, providing a numerically well conditioned quantity for solving flows

under gravitational effects. Below `alpha.oil` are the boundary conditions that influence the local oil level within each computational cell. The `RotatingWallVelocity` boundary condition is employed for the purpose of effecting rotations around their own axes (spin). In order to facilitate the rotation of the fluid from the oil bath, a Multiple-Reference Frame (MRF) zone is utilised.

Table 4. Boundary Conditions for 22320.

Component	U	p_rgh	alpha.oil
Inner ring	RotatingWallVelocity	zeroGradient	zeroGradient
Outer ring	RotatingWallVelocity	zeroGradient	zeroGradient
Rolling Elements	RotatingWallVelocity	zeroGradient	zeroGradient
Cage	zeroGradient	zeroGradient	zeroGradient
Gaps	zeroGradient	zeroGradient	zeroGradient
Front/Back wall	MRFnoSlip	fixedValue	zeroGradient

Initially, a mesh convergence study is conducted. In this instance, the mesh is gradually refined, with the total loss moment being determined as a consequence. The operating point for all simulations during the mesh study was set at 1920 rpm, 50 °C, and half shaft in oil. It is hypothesised that the mesh fineness determined with 1920 rpm is adequate for the simulations conducted at 960 rpm. The result is displayed in Figure 7. A systematic mesh refinement study was performed using grids of 6.263, 8.192, 10.617, 12.124, and 15.912×10^6 cells. The quantity of interest was the predicted hydraulic torque. With each refinement of the mesh, the solution for the simulated hydraulic loss torque approached an asymptote. We considered the mesh with 10.617×10^6 cells to be sufficiently resolved for engineering accuracy, as it differs by less than 3% from the next finer grid. All subsequent simulations were carried with this mesh. The properties of the mesh are delineated in Table 5. A detailed view of the cells used after the mesh convergence study is given in Table 5.

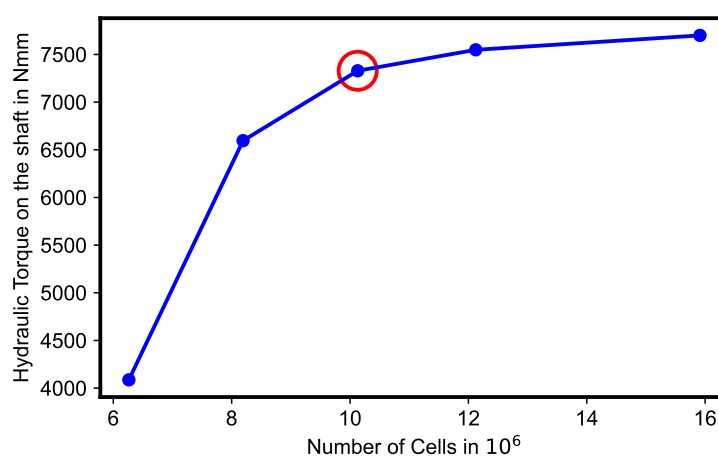


Figure 7. Mesh study for bearing 22320: simulated hydraulic torque over number of cells for 1920 rpm, 50 °C, and half shaft in oil. The dots denote the simulations that were conducted, red circle designates the mesh that was selected.

Table 1 summarizes the nine operating points investigated in the CFD campaign. The combinations of inner-ring rotational speed (960 and 1920 rpm), bulk oil temperature (50 and 70 °C), and static oil fill level (13.5, 46, and 92 mm) were chosen to match conditions for the experimental measurements from MEGT. These data are subsequently used to validate the numerical model. The prescribed oil temperature sets the thermophysical

properties applied in the simulations—most notably the viscosity of the lubricant and, via temperature-dependent correlations, the viscosity (and density) of the entrained air phase. The three oil levels represent distinct filling states: 13.5 mm corresponds to a level reaching the midline of the lowest rolling element, 46 mm corresponds to approximately one quarter of the shaft diameter, and 92 mm corresponds to a level at which roughly half of the shaft diameter is submerged in oil.

Table 5. Properties of the mesh used for the CFD simulations.

Mesh	Values
Points	13,803,361
Faces	34,892,732
Cells	10,617,940
Max cell openness	3.81189×10^{-16}
Max aspect ratio	22.6224
Average mesh non-orthogonality	18.5336
Max skewness	3.90948

2.2.2. Governing Equations

The relevant equations for calculating changes in the flow field are the Navier–Stokes equations. These consist of mass (see Equation (1)) and momentum conservation (see Equation (2)). For simulating two-phase flow (oil and air), the Volume of Fluid equation (see Equation (3)) is also solved. In this work, the bearing is modelled as isothermal; therefore, the energy equation was not included in the calculation, and the temperature was considered as a constant lubricant property. The interFOAM solver is utilised for this particular application. The solver is employed to solve the Navier–Stokes equations for two incompressible, isothermal, immiscible fluids. The equations simplify to the following [24]:

$$\nabla \vec{u} = 0, \quad (1)$$

$$\rho \left(\frac{\partial \vec{u}}{\partial t} + \nabla \vec{u} \vec{u} \right) = -\nabla p + \mu \nabla^2 \vec{u} + \vec{f}, \quad (2)$$

$$\frac{\partial \alpha}{\partial t} + \nabla \alpha \vec{u} = 0, \quad (3)$$

where \vec{u} is the velocity vector of a particle in metres per second ($\frac{m}{s}$), ρ describes the density of the mixture of oil and air in kilograms per cubic metre ($\frac{kg}{m^3}$), p is the pressure in pascals Pa, μ is the dynamic viscosity of the mixture of oil and air in Pascal seconds (Pa·s), and α represents the volume fraction. \vec{f} is a source term for forces; in our simulation setup, this includes the source terms for the coriolis force and centrifugal force of the MRF method. These Equations can be solved using the PIMPLE algorithm [25]. In order to obtain the individual hydraulic losses, the individual torques and therefore forces are necessary. In essence, two forces are of particular relevance: The force acting tangentially (\vec{F}_t) on the surface of a component, which results in the churning losses and the force acting on the surface in the normal vector (\vec{F}_n), resulting in the drag losses. The tangential force is determined by integrating the shear (τ) over the surface of the component, while the normal vector force is determined by integrating the pressure (p) over the surface [1]:

$$\vec{F}_t = \int_A \tau \cdot \vec{n} dA, \quad (4)$$

$$\vec{F}_n = \int_A p \cdot \vec{n} dA. \quad (5)$$

It can be determined by multiplying the forces by the corresponding radius that the loss moments of the individual rolling bearing components can be ascertained. The tangential force counteracts the rotation of a component. The moment caused by churning is calculated by offsetting this against the component radius. The force resulting from the pressure counteracts the translational movement of the components and is therefore only relevant for the rolling elements. The calculation of this force, with respect to the distance from the shaft axis, enables the determination of the drag torque of the rolling elements. In experimental settings, the measurement of torque loss on the shaft is the metric that can be used for validation. In order to facilitate a comparison between the simulation data and the experimental data, the hydraulic loss torque (M_{hydr}), which is measured at the shaft, is calculated. In the experimental setup, the hydraulic loss torque is calculated by subtracting the load-dependant loss torque (M_{min}), which is measured by the minimal fill height of oil from the measured (total) loss torque (M_{total}), seen in Equation (6).

$$M_{hydr} = M_{total} - M_{min}. \quad (6)$$

The hydraulic loss torque in the simulation is calculated using a power balance between the components of the bearing and the shaft. The hydraulic loss torque is equal to the total power loss simulated in the CFD simulation divided by the shaft's rotational speed (which is equal to the rotational speed of the inner ring ω_{IR}). The total power loss can be described as power loss resulting from the churning (P_{churn}) and the power loss resulting from drag (P_{drag}). The resulting equation is shown in Equation (7):

$$M_{hydr} = \frac{P_{churn} + P_{drag}}{\omega_{IR}}. \quad (7)$$

Power loss induced from the drag losses of the rolling elements are calculated with the drag torque ($M_{Re,drag}$) and the speed of the cage (ω_{Ca}):

$$P_{drag} = \omega_{Ca} \cdot M_{Re,drag}. \quad (8)$$

Power loss induced from the churning losses is a sum of the individual power losses from the rolling elements ($P_{Re,churn}$), the cage ($P_{Ca,churn}$), and the inner ring ($P_{IR,churn}$). The individual power losses are calculated by multiplying the individual churning loss torque with the corresponding component speed.

$$P_{churn} = P_{Re,churn} + P_{Ca,churn} + P_{IR,churn}, \quad (9)$$

with

$$P_{Re,churn} = \omega_{RE} \cdot M_{Re,churn},$$

$$P_{Ca,churn} = \omega_{Ca} \cdot M_{Ca,churn},$$

$$P_{IR,churn} = \omega_{IR} \cdot M_{IR,churn}.$$

All surface speeds are inputs for the CFD simulation as boundary conditions. The inner-ring speed is specified based on the MEGT experiments. The absolute angular speed of the rolling element ω_{Re} and the cage ω_{Ca} are determined by reference to Equations (10) and (11), where d_m is the diameter to the centre point of the rolling element and d_{Re} refers to the diameter of the rolling element.

$$\omega_{Re} = -\frac{\omega_{IR}}{2} \cdot \left(\frac{d_m}{d_{Re}} - \frac{d_{Re}}{d_m} \right), \quad (10)$$

$$\omega_{Ca} = \frac{\omega_{IR}}{2} \cdot \left(1 - \frac{d_{Re}}{d_m}\right). \quad (11)$$

2.2.3. Determination of Quasi-Stationary Conditions

For all CFD simulations, the target state is (quasi) steady: the hydraulic force F_{hydr} and hydraulic torque M_{hydr} acting on the components exhibit no drift in time. To verify this, both quantities are monitored over the number of revolutions of the rolling-element set, which in this case means that the rolling elements have returned to their initial position after one rotation around the shaft. The duration of such a revolution depends on the speed of the rolling-element set and thus indirectly on the speed of the inner ring. At an inner-ring speed of 960 rpm, one revolution of the rolling-element set takes 0.155 s. A simulation is terminated once no further change is detectable within a prescribed tolerance ($\delta < 0.05$) over multiple successive revolutions. In practice, this amounts to 3–5 revolutions. The example in Figure 8 was stopped after 3.2 revolutions.

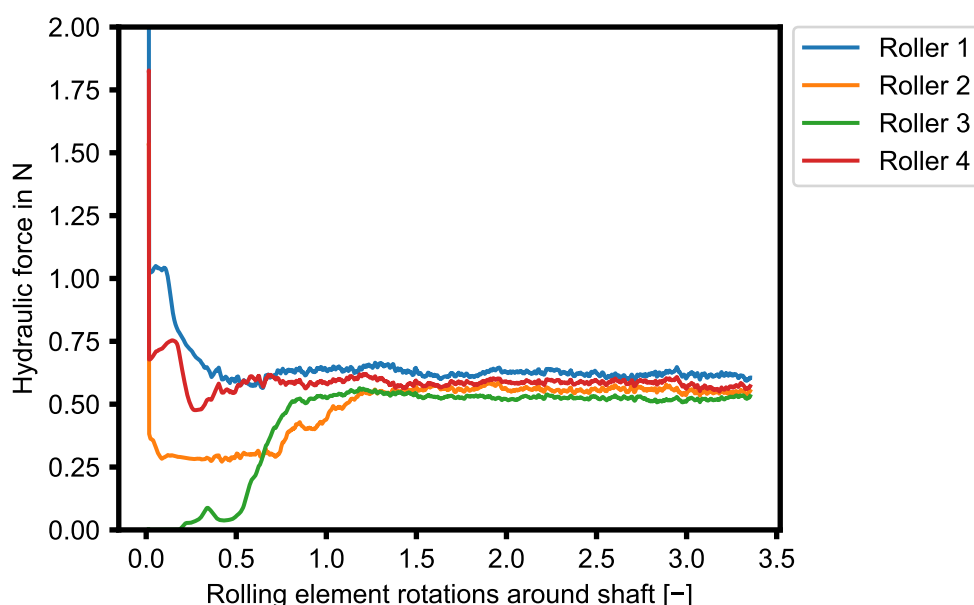


Figure 8. Hydraulic force over rotations of the rolling-element set, for 960 rpm inner-ring speed, 50 °C oil temperature, and 96 mm oil fill level.

Figure 8 illustrates the evolution of F_{hydr} for four representative rolling elements (Roller 1–4) at 960 rpm inner-ring speed, 50 °C oil temperature, and 96 mm oil fill level. Their initial positions relative to the oil bath are distinct: Roller 1 starts at the lowest angular position and is fully submerged. Rollers 2 and 4 are initially half submerged. Roller 3 is fully surrounded by air (see Figure 9). Upon the onset of rotation, Roller 1 must displace oil over its entire wetted surface and therefore exhibits the largest initial force. As it leaves the bath after roughly 0.25 revolutions, its force decays toward the common steady level. Roller 2 moves into the oil bath at start-up and as its level of submergence increases, the force rises until it plateaus. Roller 3, beginning in air, shows a correspondingly small initial force. Although it would nominally enter the bath after about 0.25 revolutions, the data indicate a delayed increase. This delay is consistent with a transient redistribution of lubricant within the bearing that temporarily lowers the sump level. Roller 4 moves out of the bath at start-up and its force drops to a low, nearly constant value for more than half a revolution, likely reflecting the entrained fluid that co-rotates with the element. After approximately 0.8 revolutions, it re-enters the remaining oil pool and its force rises toward the common level.

After these run-in transients, most pronounced within the first 1.5 revolutions, the four curves collapse onto a narrow band with only small stationary fluctuations, indicating a quasi-steady global load state. Minor residual differences persist, especially in the lubrication pockets between the rolling elements (see Figure 9), signaling that the free-surface distribution continues to relax even while the integrated forces are effectively steady. For this reason, we maintain the simulation until there is a constant distribution of oil inside of the bearing (here: 3.2 revolutions), with termination between three and five revolutions in the broader campaign.

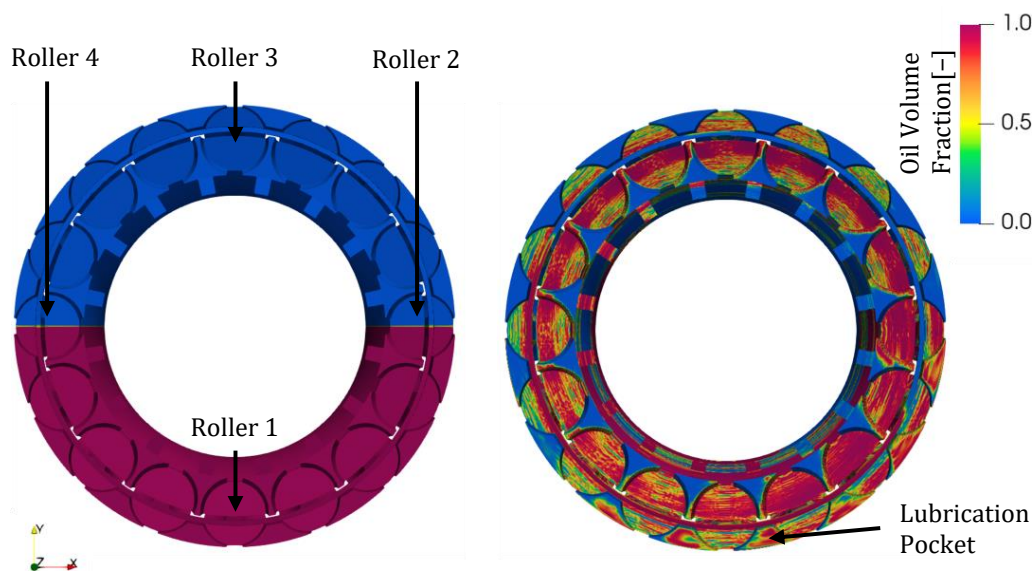


Figure 9. Oil distribution over rotations for the bearing 22320, left: start of the simulation, right: after 2 rotations of the rolling-element set; red: cell is fully filled with oil, blue: cell is fully filled with air.

3. Results

To validate the simulation model, a comparison is made between the simulated hydraulic losses and the experimentally determined hydraulic losses. In addition, the experimental and simulated results are compared with the hydraulic losses according to SKF [3]. The losses in the simulation are determined as outlined in Section 2.1. Figure 10 presents the hydraulic loss torque as a function of the oil level (13.5, 46, and 92 mm) for three operating conditions. Solid lines denote independent experiments, dashed lines show the corresponding CFD predictions, and dotted lines show the SKF predictions. The three data sets span 1920 rpm at 50 °C (blue), 960 rpm at 50 °C (yellow), and 960 rpm at 70 °C (green).

At a fixed speed and temperature, the minimum hydraulic losses are consistently observed at the lowest oil level of 13.5 mm. Utilising a rotational speed of 1920 revolutions per minute and a temperature of 50 °C, a hydraulic loss torque of 4.45 Nm was ascertained. The loss torque, as determined by the CFD simulation, exhibited a deviation of 4.25 Nm (5%) from the result. Pursuant to the SKF equation, a value of 0.55 Nm is predicted, corresponding to a deviation of 87%. The investigation revealed that, at a constant speed and oil temperature, an augmentation of the oil level to 46 mm resulted in an escalation of the hydraulic loss torque for all three curves. The experimental determination of hydraulic loss torques has revealed an increase of 6.47 Nm in comparison to the 6.05 Nm that were determined by CFD simulation. In this context, a discrepancy of (7%) was identified between the results of the CFD simulation and the experimental measurements. According to SKF, the hydraulic loss torque is 2.48 Nm, thereby reducing the deviation to (62%). The highest oil level that was examined, 92 mm, resulted in a significant increase in the hydraulic loss

torque in all three considerations. This increase is accompanied by a concurrent reduction in the slope of the increase, as evidenced by both the experimental evaluation and the CFD simulation, in comparison to the results of the preceding oil increase. In the experimental study, a hydraulic loss torque of 7.4 Nm was determined, while the CFD simulation yielded a result of 7.32 Nm. This is equivalent to a deviation of (2%). In accordance with the SKF equation, the hydraulic loss torque is calculated to be 4.32 Nm, which corresponds to a deviation of (52%) in comparison with the experimental results.

Analogue curves can be observed for all curves at 960 revolutions per minute and at 50 and 70 °C. It was found that an increase in the oil level is accompanied by an increase in hydraulic losses. At the same time, it was observed that the slope decreases as the oil level increases. The exception to this is the measuring point at 960 revolutions per minute, 50 °C, and an oil level of 92 mm. The CFD simulation shows a discrepancy in the evaluation of the hydraulic torque compared to the experimental results. At a rotational speed of 960 revolutions per minute, a temperature of 70 °C and an oil level of 13.5 mm, the hydraulic torque is underestimated by (4%). At a rotational speed of 960 revolutions per minute, a temperature of 50 °C, and an oil level of 92 mm, an overestimation of the hydraulic torque of (20%) is observed. The deviation from the SKF equation is significantly greater, reaching a value of (90%) in some cases (960 revolutions per minute, 70 °C, 13.5 mm oil level).

At a constant speed (960 rpm), elevating the oil temperature from 50 °C to 70 °C decreases the hydraulic loss torque. In the CFD results, this reduction is nearly uniform at ≈ 17 – 18% across all investigated fill levels. Conversely, at a fixed oil temperature and fill level, increasing speed always increases the hydraulic loss torque, consistently in both experimental, SKF, and CFD datasets.

Figure 11 and Table 6 report the total hydraulic loss torque and the percentage contribution of each component to the total fluid-dynamic loss for the nine operating points, expressed as shares of the simulated hydrodynamic loss torque at each condition. Across all operating points, churning at the rolling elements is the leading contributor (≈ 45 – 60%), followed by churning at the inner ring (≈ 21 – 43%) and rolling-element drag (≈ 8 – 30%). Cage-related losses remain consistently small (≈ 0.5 – 2.0%). Increasing the oil fill level generally shifts the distribution toward a higher rolling-element drag and slightly larger cage shares, while the ring churning share declines. A temperature increase from 50 °C to 70 °C at 960 rpm primarily redistributes shares at higher fill heights, reducing inner churning fractions and elevating rolling-element drag. The churning losses of the rolling elements are the dominant loss. Doubling the speed from 960 to 1920 rpm at 50 °C shifts shares from rolling-element churning toward inner-ring churning. The rolling-element drag share simultaneously decreases. In summary, losses associated with the rolling elements dominate under all conditions, ring churning becomes relatively more important at higher speeds (especially at lower oil levels), and higher fill levels favor rolling-element drag while suppressing ring churning. Temperature changes mainly reallocate shares without altering this overall hierarchy.

Table 6. Individual percentage loss shares of the individual components of the spherical roller bearing 22320.

Operation Point	Drag Re [% Nm]	Churning Re [% Nm]	Churning IR [% Nm]	Churning Ca [% Nm]
1	13.45 0.296	60.15 1.323	25.09 0.552	0.66 0.015
2	24.31 0.729	45.76 1.373	27.67 0.830	1.14 0.034
3	21.97 0.769	47.28 1.655	26.87 0.940	1.93 0.068
4	10.76 0.161	59.96 0.899	27.79 0.417	0.76 0.011

Table 6. Cont.

Operation Point	Drag Re [% Nm]	Churning Re [% Nm]	Churning IR [% Nm]	Churning Ca [% Nm]
5	26.28 0.557	47.52 1.007	36.44 0.773	0.98 0.021
6	29.57 0.710	44.72 1.073	21.65 0.520	2.03 0.049
7	7.6 0.319	47.57 1.998	43.8 1.840	0.52 0.022
8	18.63 1.117	45.45 2.727	34.55 2.073	0.69 0.041
9	22.72 1.658	46.13 3.368	28.97 2.115	1.01 0.074

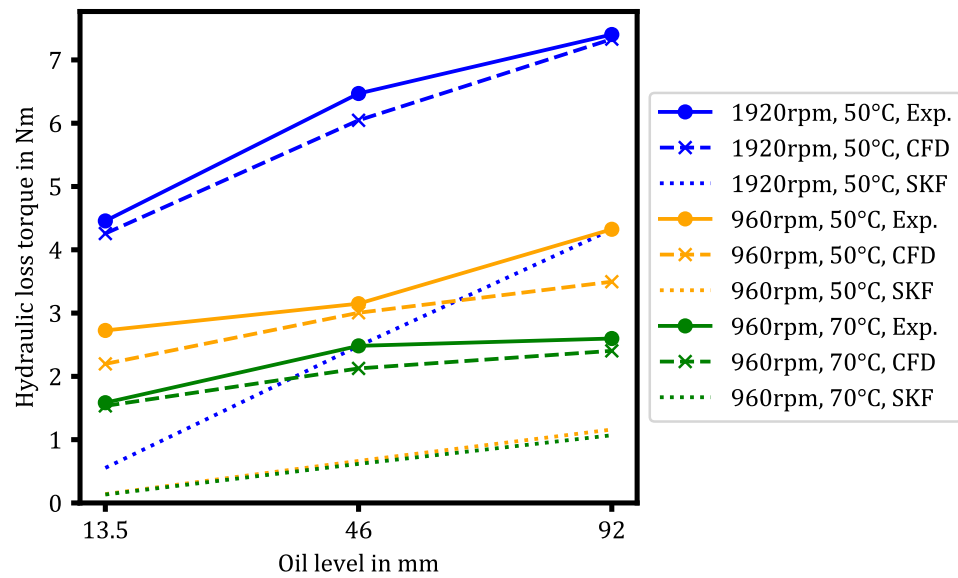


Figure 10. Hydraulic losses via oil level for spherical roller bearing 22320 at 960 rpm and 70 °C: yellow, 960 rpm and 50 °C: green, 1920 rpm and 50 °C: blue.

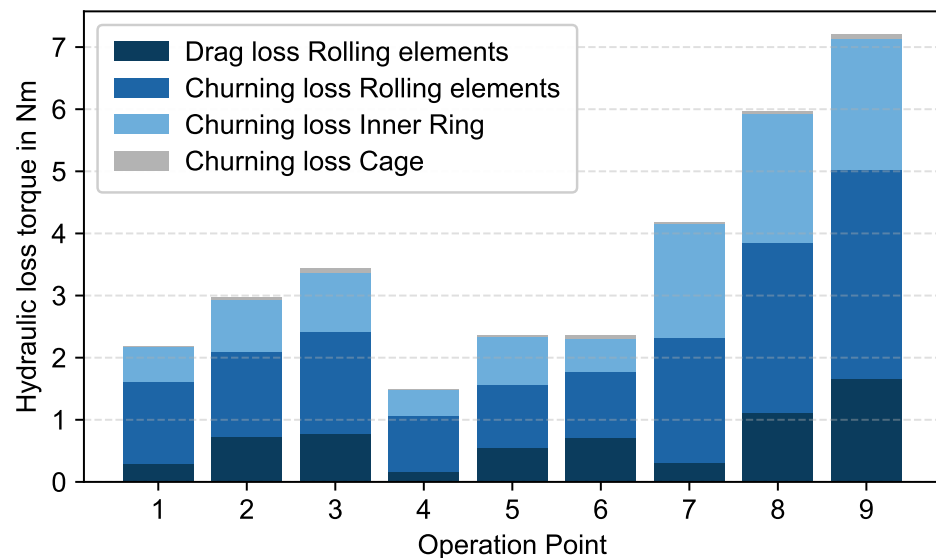


Figure 11. Total and Individual percentage loss shares of the individual components of the spherical roller bearing 22320 for the 9 operation points.

4. Discussion

The relative ordering of the curves shown in Figure 10 is physically consistent. At a fixed temperature (50 °C), doubling the speed from 960 to 1920 rpm produces an increase

in torque at every fill height, as higher speeds increase shear forces on surfaces in the partially flooded bearings. At a fixed speed (960 rpm), raising the oil temperature from 50 to 70 °C lowers the torque across the board, which results from the decrease in lubricant viscosity and the associated reduction in shear and free-surface damping. Taken together, these trends show that (i) fill level controls the effective immersion and therefore the bulk of churning work, (ii) rotational speed amplifies those losses strongly, and (iii) temperature, via viscosity, modulates the magnitude of all contributions without changing the qualitative behaviour. The CFD reproduces the key features of the measurements, such as the monotonic increase with fill height, the strong speed effect, and the systematic reduction at higher temperatures. Quantitatively, the simulations exhibit a consistent negative bias (under-prediction) relative to the experiment, most visible at low to moderate speed/temperature combinations, while agreement tightens at the warmest case and highest fill. Possible sources of the residual gap include geometric simplifications, closing lubrication gaps, uncertainties in the degree of heating of the fluid due to internal friction for oil and air, and the treatment of rotating zones (e.g., MRF versus fully transient motion). Despite these factors, the overall correspondence in trends and the stable ordering of the curves indicate that the CFD captures the governing dependencies on fill height, speed, and temperature with enough fidelity. Compared to the SKF equation, the CFD simulation shows a significant improvement (in some cases by a factor of 10 of the percentage deviation) in the accuracy of estimating hydraulic losses for the 22320 spherical roller bearing. The SKF equation underestimates hydraulic losses by at least 52%.

The predominance of rolling elements in the hydraulic loss torque can be attributed to their multiplicity and cumulative area, which together amplify both viscous shear and fluid displacement. The observation that churning exceeds drag is consistent with kinematics: the self-rotation of the rollers typically yields higher surface velocities than their orbital motion about the shaft axis, increasing shear-driven dissipation. Drag, in contrast, is concentrated during immersion events at the oil bath/free surface and when rollers traverse regions of bulk fluid.

At low fill levels (e.g., 13.5 mm), the lubricant is spread thinly over a large portion of the bearing, leaving only a small to no lubrication sump. This promotes extensive surface wetting with limited free volume, favoring shear-dominated (churning) losses over displacement-dominated (drag) losses. As the fill level increases from 13.5 to 46 mm, a larger free oil volume develops. The resulting bulk fluid is more effectively displaced by roller motion, increasing the drag contribution. This mechanism explains the measured rise in the drag fraction, by as much as 16 percentage points, between operating points 1 → 2, 4 → 5, and 7 → 8.

At present, experimental validation is limited to the total hydraulic loss torque. Component-resolved losses cannot be verified experimentally with the available setup. Accordingly, the component-level results reported here should be interpreted as indicative rather than definitive.

Because comparative data for spherical roller bearings are scarce, we benchmark our results from the individual hydraulic losses (see Table 6) against two studies that reported component-resolved hydraulic losses: FELDERMANN [1] and LIEBRECHT [4]. A one-to-one comparison between our results and those of LIEBRECHT and FELDERMANN is not appropriate due to differences in bearing type and test configuration (axial tapered roller bearing in LIEBRECHT and radial cylinder roller bearings in FELDERMANN versus radial spherical roller bearing in the present study). Nevertheless, the aim of this comparison is to provide an initial assessment of the significance of individual losses, as these cannot currently be validated on an individual basis.

FELDERMANN simulated a fully filled radial cylindrical roller bearing. Across all operating points, the churning losses of the rolling elements were the dominant contribution ($\approx 57\%$). Cage churning losses were minor ($\approx 1\%$). Inner-ring losses were similar to the present work ($\approx 30\%$), while overall drag losses were lower ($\approx 10\%$) than those obtained in our simulations. LIEBRECHT is among the few authors to publish individual loss contributions. Investigating axial tapered roller bearings, he found that the dominant mechanism was not churning but drag on the rolling elements, accounting for $\approx 39\text{--}46\%$ of total losses, whereas churning of the rolling elements contributed only $\approx 8\text{--}9\%$. Churning losses of the inner ring ($\approx 14\text{--}15\%$) were lower, as in our study. [1,4].

In LIEBRECHT's setup, the shaft is oriented vertically (parallel to gravity) and tests include a fully flooded reference condition in which the oil initially envelops the entire bearing cross-section (fully flooded level \approx three times the bearing width). The tapered geometry produces a pronounced pumping effect that drives the lubricant axially upward against gravity. The test housing was even modified with grooves to return the oil and compensate this effect. Under these conditions, the rolling elements remain immersed over a large portion of their path, which elevates drag (pressure) contributions. Consistent with this mechanism, their CFD-based component breakdown shows the rolling elements dominating the hydraulic losses ($\approx 45\%$ inertial plus $\approx 9\%$ viscous across 2000–6300 rpm), while cage viscous losses are $\approx 1\%$ and inner/outer viscous losses are $\approx 36\text{--}38\%$.

The combination of (i) axial TRB geometry with vertical orientation and sustained upward pumping/through-flow versus (ii) radial SRB geometry with a bottom oil pool provides a coherent explanation for the higher drag losses reported by LIEBRECHT relative to our simulations. This interpretation is consistent with later summaries noting that, for TRBs with a vertically oriented shaft, oil level and the resulting through-flow strongly amplify drag and churning losses, especially at higher speeds.

FELDERMANN's work focuses on load-independent hydraulic losses in a radial CRB and employs a CFD workflow that resolves the global flow and then maps it to a rotating-frame chamber model for componentwise loss estimation. This setup represents a fully flooded or oil-bath regime in which the rolling elements and cage remain continuously immersed. These differences in geometry and flooding modify the dominant flow mechanisms around the rolling elements and help explain the observed deviation in drag losses. In a fully flooded CRB, the oil mass in the pockets and clearances is strongly entrained by rotation, promoting quasi-solid-body co-rotation of the fluid and thereby reducing the relative velocity at the roller surface. That tends to suppress the rolling-element drag component (per unit wetted area) while increasing bulk churning losses, because a larger oil volume is accelerated continuously.

By contrast, in our SRB, the oil accumulates primarily in the lower sector. The elements cyclically enter and exit the bath, and the spherical raceways drive three-dimensional secondary flows and free-surface interactions. The repeated wetting/dewetting, local accelerations at the free surface, and the more three-dimensional cross-flow increase pressure and viscous drag on the rolling elements relative to a fully flooded state. This flooding-level sensitivity of drag/churning partitioning is widely reported in the bearing CFD literature and full-flooded experiments [26].

Overall, while a strict quantitative match is neither expected nor intended, the differences in drag are physically consistent with the respective bearing types, orientations, and lubrication fill states. In this context, the churning losses of the rolling elements are to be regarded as the dominant factor. Compared to the current kinematic simulations, a considerably stronger deceleration of the rolling-element speed can be expected after the hydraulic losses are implemented. The present study concludes that, due to the predomi-

nant churning losses of the rolling elements, a significant reduction in the rolling-element speed in the kinematic simulation can be expected as soon as the load zone is left.

5. Conclusions

The present study examined the three overarching tasks for the 22320 spherical roller bearing: 1. Resolve hydraulic losses at the component level (rolling elements, inner ring, cage) by separately quantifying drag and churning. 2. Validate total hydraulic losses against experiments. 3. Assess the influence of operating parameters of the inner-ring speed, lubricant temperature, and fill level on the distribution and magnitude of hydraulic losses.

The CFD model developed for the 2320 spherical roller bearing captures the trend of change with different operating conditions and reproduces the measured total hydraulic losses with high fidelity (deviation of 2–7%). A notable exception occurs at 50 °C, where the deviation from the measurements is substantially larger (5–19%). This is plausibly attributable to uncertainty in the experimental temperature determination, as the corresponding data series exhibits a trend inconsistent with the other temperature levels. Given the overall agreement, the modelling simplifications adopted here appear justified. Across all operating points, rolling-element churning was the dominant contribution (45–60% of total hydraulic losses), followed—depending on the operating point—by either the rolling-element drag or inner-ring churning, and cage churning was consistently the lowest.

Within the investigated parameter space, the inner-ring speed (and thus the circumferential velocity of the rolling elements) is the primary driver of the hydraulic power loss. An increase in oil fill level also raises these losses, but with diminishing sensitivity: small increments at low fill produce disproportionately large changes due to the rapid growth of the wetted area and entrained fluid mass, whereas at higher fill levels, additional oil mainly augments the bulk volume with comparatively minor changes in shear-producing interfaces. Oil temperature influences through viscosity. At elevated temperatures, the dynamic viscosity μ decreases, which reduces the dominant churning component and partially offsets the increases caused by speed and fill level. In summary, speed is the dominant control, fill level exhibits a saturating effect, and temperature (via μ) moderates the losses, primarily by attenuating churning.

The results reported in this study are limited to the 22320 spherical roller bearing and to the investigated parameter space. Based on the current state of knowledge, the quantified contributions of the individual hydraulic loss components cannot be directly extrapolated to other bearing sizes or to operating conditions outside the considered range. Further modelling limitations should be noted: constant viscosities were assumed for both oil and air, implying an isothermal lubricant with no shear-thinning behaviour. Moreover, the flow within the lubrication gap is not resolved, and the interaction between the oil flow and adjacent surrounding geometries is not represented.

Future work should extend CFD analyses of spherical roller bearings to a broader range of operating conditions and geometries to obtain a more detailed understanding of the behaviour of drag and churning losses. The evidence base for component-resolved hydraulic losses remains limited. Targeted studies that vary bearing size and consider available envelope and housing constraints are needed. In addition, a methodological comparison between two modelling strategies, i.e., (i) closing lubrication gaps and (ii) virtually shrinking the rolling elements to impose clearance, should be conducted to quantify their impact on predicted loss partitions. Ultimately, this line of work enables the component-specific implementation of hydraulic losses in kinematic simulations, with the aim of improving the accuracy of kinematic predictions. In the next step, the hydraulic losses are incorporated into a multibody simulation, which is then used to simulate the bearing kinematics under the operating conditions investigated in this work. Agreement between

simulated and experimentally measured kinematics indicates that the individual hydraulic losses have been captured with the correct order of magnitude.

Author Contributions: T.C.P.: writing—original draft, writing—review and editing, visualization, methodology, numerical investigation, project administration, data curation, and conceptualization. K.M.B.: writing—original draft, writing—review and editing, visualization, methodology, experimental investigation, project administration, data curation, and conceptualization. G.J.: writing—review and editing, supervision, project administration, funding acquisition, and conceptualization. O.K.: writing—review and editing, supervision, project administration, funding acquisition, and conceptualization. B.L.: writing—review and editing, supervision, project administration, and conceptualization. P.R.: writing—review and editing, supervision, and conceptualization. A.N.: writing—review and editing, investigation, and conceptualization. All authors have read and agreed to the published version of the manuscript.

Funding: This research was funded by the Deutsches Zentrum für Luft- und Raumfahrt (DLR) and the Forschungsvereinigung Antriebstechnik e.V. (FVA) under FVA project 830 II, grant number 23040 N. We also acknowledge support from the Bundesministerium für Wirtschaft und Energie (BMWE).

Data Availability Statement: The data presented in this study are available on request from the corresponding author. The data are not publicly available due to privacy.

Acknowledgments: Computations were performed with computing resources granted by RWTH Aachen University under project rwth1722.

Conflicts of Interest: The authors declare no conflicts of interest. The funders had no role in the design of the study; in the collection, analyses, or interpretation of data; in the writing of the manuscript; or in the decision to publish the results.

References

1. Feldermann, A.; Fischer, D.; Neumann, S.; Jacobs, G. Determination of hydraulic losses in radial cylindrical roller bearings using CFD simulations. *Tribol. Int.* **2017**, *113*, 245–251. [[CrossRef](#)]
2. Braendlein, J. Die Waelzlagerpraxis. Handbuch fuer die Berechnung und Gestaltung von Lagerungen. In *Mainz: Vereinigte Fachverlage*; Verlag R. Oldenbourg: München, Germany, 1995.
3. SKF. *The SKF Model for Calculating the Frictional Moment*; Document Code: PM CTP CAT D A5 X 3 v01 (2009-06-07); Technical Note; SKF Group: Gothenburg, Sweden, 2009.
4. Liebrecht, J.; Si, X.; Sauer, B.; Schwarze, H. Investigation of Drag and Churning Losses on Tapered Roller Bearings. *Stroj. Vestn. J. Mech. Eng.* **2015**, *61*, 399–408. [[CrossRef](#)]
5. Zhou, R.S.; Hoepflich, M.R. Torque of Tapered Roller Bearings. *J. Tribol.* **1991**, *113*, 590–597. [[CrossRef](#)]
6. Kim, K.S.; Lee, D.W.; Lee, S.M.; Lee, S.J.; Hwang, J.H. A numerical approach to determine the frictional torque and temperature of an angular contact ball bearing in a spindle system. *Int. J. Precis. Eng. Manuf.* **2015**, *16*, 135–142. [[CrossRef](#)]
7. Wang, D. *Berechnung der Wälzlagerreibung Aufgrund Weiterentwickelter Rheologischer Fluidmodelle*; Gottfried Wilhelm Leibniz Universität Hannover: Hannover, Germany, 2015. [[CrossRef](#)]
8. SKF Group. *Rolling Bearing Catalog PUB BU/P1 17000/1 EN*; SKF Group: Gothenburg, Sweden, 2018.
9. Peterson, W.; Russell, T.; Sadeghi, F.; Berhan, M.T. Experimental and analytical investigation of fluid drag losses in rolling element bearings. *Tribol. Int.* **2021**, *161*, 107106. [[CrossRef](#)]
10. Gao, W.; Lyu, Y.; Liu, Z.; Nelias, D. Validation and application of a numerical approach for the estimation of drag and churning losses in high speed roller bearings. *Appl. Therm. Eng.* **2019**, *153*, 390–397. [[CrossRef](#)]
11. Sadeghi, F.; Arya, U.; Aamer, S.; Meinel, A. A Review of Computational Fluid Dynamics Approaches Used to Investigate Lubrication of Rolling Element Bearings. *J. Tribol.* **2024**, *146*, 100801. [[CrossRef](#)]
12. Maccioni, L.; Concli, F. Computational Fluid Dynamics Applied to Lubricated Mechanical Components: Review of the Approaches to Simulate Gears, Bearings, and Pumps. *Appl. Sci.* **2020**, *10*, 8810. [[CrossRef](#)]
13. Gao, W.; Zhang, S.; Li, X.; Liu, Z. Investigation on the drag effect of a rolling element confined in the cavity of a cylindrical roller bearing. *Proc. Inst. Mech. Eng. Part J J. Eng. Tribol.* **2022**, *236*, 777–785. [[CrossRef](#)]
14. Marchesse, Y.; Changenet, C.; Ville, F. Drag Power Loss Investigation in Cylindrical Roller Bearings Using CFD Approach. *Tribol. Trans.* **2019**, *62*, 403–411. [[CrossRef](#)]

15. Maccioni, L.; Chernoray, V.G.; Concli, F. Investigating lubricant behavior in a partially flooded tapered roller bearing: Validation of a multiphase CFD solver for aerated oil sump via particle image velocimetry studies and high-speed camera acquisitions. *Tribol. Int.* **2025**, *201*, 110274. [[CrossRef](#)]
16. Concli, F.; Schaefer, C.T.; Bohnert, C. Innovative Meshing Strategies for Bearing Lubrication Simulations. *Lubricants* **2020**, *8*, 46. [[CrossRef](#)]
17. Aul, E. Analyse von Relativbewegungen in Wälzlagersitzen. Ph.D. Thesis, TU Kaiserslautern, Kaiserslautern, Germany, 2008.
18. Kiekbusch, T. Strategien Zur Dynamischen Simulation von Wälzlagern. Ph.D. Thesis, TU Kaiserslautern, Kaiserslautern, Germany, 2016.
19. Mármol Fernández, M. Development of a New Bearing Geometry to Reduce Friction Losses. Ph.D. Thesis, TU Kaiserslautern, Kaiserslautern, Germany, 2022.
20. Sebteini, S.; Hudak, R. Mindestlast von Wälzlagern. In *Abschlussbericht zum Forschungsvorhaben Nr. 830 I (Heft 1504)*; FVA Forschungsvereinigung Antriebstechnik e.V.: Frankfurt am Main, Germany, 2022.
21. Kiekbusch, T.; Sauer, B. Calculation of the Dynamic Behavior of Rolling Bearings with Detailed Contact Calculations. In *Proceedings of the EUROMECH Colloquium 578-Rolling Contact Mechanics for Multibody System Dynamics*, Funchal, Madeira, Portugal, 10–13 April 2017.
22. Wingertszahn, P.; Koch, O.; Maccioni, L.; Concli, F.; Sauer, B. Predicting Friction of Tapered Roller Bearings with Detailed Multi-Body Simulation Models. *Lubricants* **2023**, *11*, 369. [[CrossRef](#)]
23. Schwarze, H.; Poll, G.; Bartel, D. Tribologische Fluidmodelle für Nebenaggregate in Elektro- und Hybridfahrzeugen. *Mot. Z.* **2017**, *78*, 70–75. [[CrossRef](#)]
24. OpenFOAM Wiki Contributors. InterFoam. Available online: <https://openfoamwiki.net/index.php/InterFoam> (accessed on 11 September 2025).
25. OpenFOAM Guide/The PIMPLE Algorithm in OpenFOAM—OpenFOAMWiki. Available online: https://openfoamwiki.net/index.php/OpenFOAM_guide/The_PIMPLE_algorithm_in_OpenFOAM (accessed on 1 October 2025).
26. Maccioni, L.; Rüth, L.; Koch, O.; Concli, F. Load-Independent Power Losses of Fully Flooded Lubricated Tapered Roller Bearings: Numerical and Experimental Investigation of the Effect of Operating Temperature and Housing Wall Distances. *Tribol. Trans.* **2023**, *66*, 1078–1094. [[CrossRef](#)]

Disclaimer/Publisher’s Note: The statements, opinions and data contained in all publications are solely those of the individual author(s) and contributor(s) and not of MDPI and/or the editor(s). MDPI and/or the editor(s) disclaim responsibility for any injury to people or property resulting from any ideas, methods, instructions or products referred to in the content.